On the Estimation of Melt Pond Fraction on the Arctic Sea Ice With ENVISAT WSM Images

Marko Mäkynen, *Member, IEEE*, Stefan Kern, Anja Rösel, and Leif Toudal Pedersen

***Abstract*—The accuracy of microwave radiometer ice concentration (IC) retrievals in the Arctic is degraded by melt ponds on sea ice during the melting season. For the development of IC retrieval algorithms and for the quantification of their uncertainties, data sets on the area fraction of melt ponds (f_{mp}) are needed. f_{mp} retrieval with optical satellite data is limited by clouds. Thus, we have studied f_{mp} retrieval with ENVISAT wide swath mode (WSM) synthetic aperture radar (SAR) images which have large daily coverage over the Arctic Sea ice in 2007–2012. The WSM images used here were acquired north of the Fram Strait in June–August 2009. Data on f_{mp} were available from the Integrated Climate Data Center's daily Moderate Resolution Imaging Spectroradiometer (MODIS) f_{mp} product in a 12.5-km grid. Relationships between SAR σ° and MODIS f_{mp} were studied visually by comparing daily SAR mosaics and f_{mp} charts and by analyzing f_{mp} and σ° time series and spatially and temporally coincident f_{mp} and σ° data. The correspondence between the changes of f_{mp} and the σ° statistics is too low to suggest f_{mp} estimation from the WSM images. In some cases, there was a 2–3-dB σ° increase during the ponding period. It is assumed that the variation of snow and sea ice characteristics diminishes σ° changes due to the melt ponding and drainage. Good correlation between σ° and f_{mp} has only been observed for smooth landfast first-year ice in previous studies. A very interesting observation was the large temporal σ° variations during the late melting season, which are likely linked to the atmospherically forced freezing–melting events. These events may also influence radiometer IC retrievals.**

***Index Terms*—Arctic, melt ponds, radar remote sensing, sea ice.**

I. Introduction

DURING the summer time, snow and sea ice melting cause the formation of the melt ponds on the Arctic sea ice [1]. These ponds reduce the surface albedo of the sea ice cover substantially and therefore enhance summer melt. Melt enhancement on melt-pond-covered sea ice is not only caused by the reduced surface albedo but also by the increased penetration of solar radiation through the sea ice, as well as via enhanced lateral sea ice melt at the melt pond edges [1], [2]. Melt ponds are typically interconnected on first- and second-year sea ice but discrete on multiyear ice (MYI) or heavily deformed ice due to topography [3]. The size of melt ponds ranges over two orders of magnitude; small melt ponds with a size below 50 m^2 are found to be most common [4].

The accuracy of microwave radiometer ice concentration (IC) retrievals is reduced by the presence of wet snow and ice, by temporary thin ice layers on the top and within the near-surface snow/ice volume due to night freeze, and especially by melt ponds on sea ice, e.g., [5]. For the development of IC retrieval algorithms and for the determination and quantification of uncertainties in the summer time, IC data sets on sea ice thermodynamic state changes and the area fraction of melt ponds are needed. The inclusion of melt ponds in models has been shown to provide more realistic progress of the summer melt [6], [7].

The small size of melt ponds and prevailing cloudy conditions in summer complicate their monitoring using satellite data, e.g., [8]. Satellite microwave radiometers and scatterometers have a resolution which is too coarse, e.g., [9] and [10], while the usage of optical data is hampered by cloud cover [11], [12]. Recently, a method has been developed to estimate melt pond fraction (f_{mp}) and IC with Moderate Resolution Imaging Spectroradiometer (MODIS) surface reflectance data [8]. A MODIS f_{mp} and open water fraction (f_{ow}) product with a 12.5-km pixel size, based on the Arctic 8-day MODIS reflectance composite (MOD09A1), is available from the Integrated Climate Data Center (ICDC), University of Hamburg [13]. The 8-day MODIS reflectance composite is preferred over daily MODIS reflectance data because the method requires clear-sky conditions which usually can only be obtained with Arctic wide spatial coverage when aggregating daily MODIS reflectance data of several days—in this case 8. Daily maps of MODIS f_{mp} can be retrieved as well but usually show a larger number of gaps and are therefore difficult to use for monitoring f_{mp} at a certain location and a specific date. These daily maps are more suitable for case and intercomparison studies as the one presented in this paper. In addition, cloud masking of MODIS data is typically difficult over sea ice [14], [15]. Therefore, an alternative way to estimate f_{mp} will be beneficial.

The aim of our study is to investigate the possibility to obtain f_{mp} estimates from ENVISAT wide swath mode (WSM) synthetic aperture radar (SAR) images during the melt season in the Arctic. An f_{mp} estimation method is desirable, as the method can then be applied to the large ENVISAT WSM image archive over the Arctic Sea ice, acquired in 2002–2011, and also to RADARSAT-1 and 2 ScanSAR images acquired since 1995.

Manuscript received August 22, 2013; revised December 5, 2013 and February 25, 2014; accepted March 10, 2014. Date of publication April 7, 2014; date of current version May 30, 2014. This work was supported by the project Sea Ice Climate Change Initiative funded by the European Space Agency.

M. Mäkynen is with the Finnish Meteorological Institute, FI-00101 Helsinki, Finland (e-mail: marko.makynen@fmi.fi).

S. Kern is with the Integrated Climate Data Center, Center for Earth System Research and Sustainability (CEN), University of Hamburg, 20144 Hamburg, Germany (e-mail: stefan.kern@zmaw.de).

A. Rösel is with the Institute of Oceanography, University of Hamburg, 20146 Hamburg, Germany (e-mail: anja.roesel@zmaw.de).

L. T. Pedersen is with the Center for Ocean and Ice, Danish Meteorological Institute, 2100 Kobenhavn, Denmark (e-mail: ltp@dmi.dk).

Digital Object Identifier 10.1109/TGRS.2014.2311476

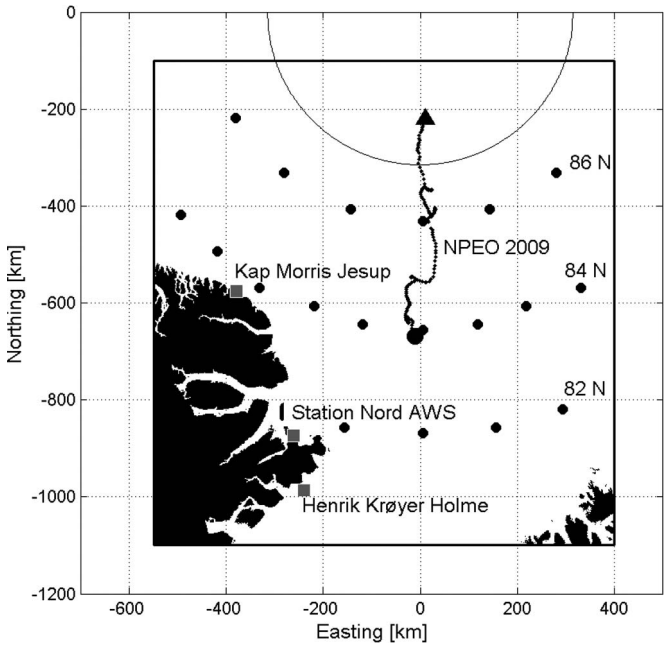

Fig. 1. Test area for the SAR-based melt pond fraction retrieval study. The rectangle shows the area, and gray squares are DMI weather stations. Dots are latitude–longitude grid points for studying the temporal behavior of the MODIS melt pond fraction and ENVISAT σ° data. The drift track of NPEO 2009 from (triangle) June 1 to (dot) August 31, 2009 is also shown. The circular line shows the extent of the ENVISAT WSM pole hole. The coordinate system is polar stereographic with a midlongitude of 0E and a true-scale latitude of 70N.

Data on f_{mp} for studying relationships between SAR backscattering coefficient (σ°) and f_{mp} are available from an ICDC's daily MODIS melt pond product (nonpublic) with a 12.5-km pixel size which was processed separately for our study with similar methods as the standard 8-day product. Our study area covers a 950 km $\times$ 1000 km rectangle north of the Fram Strait, Greenland, and Svalbard (see Fig. 1). The area is covered by first-year ice (FYI) with 30–200 cm in thickness and by MYI according to the Danish Meteorological Institute (DMI) ice charts. Additional data sets are red-green-blue (RGB) images from MODIS Level 1 B data, numerical weather model data (ERA-Interim), coastal weather station data, and International Arctic Buoy Programme (IABP) buoy data [16], as well as North Pole Environmental Observatory (NPEO) buoy data. All data sets were acquired in summer 2009.

As a background for our study, we first present hereinafter the general classification of the sea ice thermodynamic states [17], [18] and the review of relevant previous studies for our work, with the focus on the radar-based remote sensing of f_{mp}. Since useful products of thermodynamic state changes of sea ice (e.g., melt and freeze onset) based on radiometer and scatterometer data are already available, e.g., [19]–[21], and due to the lack of needed *in situ* data, we did not try to develop in this study SAR algorithms for the detection of melt and freeze onsets.

A. Sea Ice Thermodynamic States

In the literature, the annual cycle of sea ice is typically partitioned into the following thermodynamic regimes: freeze-up, winter, early melt, melt onset, and advanced melt [17], [18]. Early melt is a transition period, starting with snow pack metamorphism and ending when moisture is continuously present in the snow. At the melt onset, water in liquid phase occurs in the snow pack throughout the diurnal cycle, and the ice surface is moist. The melt onset is further divided into pendular (melt water is held in the interstices of the snow pack) and funicular (snow grain bonds break, and gravity drainage occurs) regimes. During advanced melt, the snow pack is first saturated throughout its volume and then melts rapidly, forming melt ponds and/or flooding on the ice surface. Advanced melt is divided into periods of melt ponding and pond drainage. The ponding on the ice surface occurs as long as the brine drainage networks, thaw holes, and cracks in the ice allow less water to disappear through gravity drainage than what is created by new freshwater inputs from snow melt. The gradual decrease of f_{mp} can be impeded by freeze–melt cycles, surface hydraulics, predominant winds, and precipitation events on hourly to weekly time scales, e.g., [3].

B. Previous Studies

Changes from one sea ice thermodynamic regime to another are typically reflected in the C-band copolarization σ° time series [17], [18], [22]. Aside from these thermodynamic changes, also the decrease and increase of snow volumetric wetness may have strong effects on the measured backscattering coefficient (σ°), e.g., [22]–[24]. The attenuation of propagating radar waves in the snow pack increases rapidly with increasing snow wetness, e.g., [23], which decreases the contribution of ice surface scattering and volume scattering from the porous MYI snow/ice top layer to the total scattering. For example, in a surface-based C-band scatterometer data set, both bare ice and snow-covered FYI had larger HH-polarization σ° signatures (up to 5 dB) during freezing (dry layered snow pack) than under melting (wet snow) conditions [25].

Backscattering from melt ponds (in liquid state) depends only on their surface roughness, or wind-wave spectra, which is a function of wind speed, upwind fetch, and pond depth, e.g., [26]. The fetch-induced growth of surface waves depends on the orientation, distribution, and f_{mp} of melt ponds and also on ice surface features like hummocks, which all affect the surface turbulence of wind stresses. Significant scale surface roughness has been observed for FYI melt ponds even at wind speeds of 3 m/s [26]. The measured σ° depends also on the incidence angle and the angle between the radar viewing direction and the wave orientation on the melt ponds. The modeled average C-band HH-polarized σ° with 100-m transects of *in situ* data (e.g., f_{mp}, pond depth) over FYI showed significant contributions from fetch, pond depth, and surface type variation (ponds versus hummocks) to the modeled σ° [26]. The formation of an ice skim on the melt ponds has been observed to decrease C-band copolarized σ° by up to 10 dB at small incidence angles from σ° values for ponds with rough liquid surface [25].

In general, the σ° for melt-pond-covered sea ice has been observed to be highly dynamic and the primary function of f_{mp} and surface wind speed (ponds in liquid state), e.g., [27] and [28].

Previously, estimations of f_{mp} and also integrated shortwave albedo have been studied for smooth landfast FYI within the Canadian Arctic Archipelago using RADARSAT-1 SAR images [27], [29]. Yackel and Barber [27] found a significant

positive linear relationship between σ° and f_{mp} under windy conditions (around 5.3 m/s), a weaker positive relationship under slightly lower wind speeds ($\sim$3.2 m/s), and no relationship for light wind speeds ($\sim$1.5 m/s). The range of f_{mp} determined from aircraft video data was from 13% to 34%. The incidence angle and surface wind speed explained 90% of the σ° variation during the melt pond season. There was a strong negative relationship between σ° and albedo under strong wind, a slightly weaker relationship under moderate wind speeds, and a very weak positive relationship for light wind speeds. The results also suggested that σ° may be more closely related to the albedo than to f_{mp} due to the fact that albedo results from the integration of all surface types (snow, saturated snow, and melt ponds) which contribute to the measured σ°. Hanesiak *et al.* [29] presented the albedo versus σ° relationship for the early melt period and summarized the results from earlier studies for other sea ice thermodynamic regimes. RADARSAT-1-derived surface albedo ingested into a thermodynamic sea ice model improved sea ice simulations to better predict the timing of landfast FYI breakup. Scharien *et al.* [30] demonstrated that the albedo of melt-pond-covered landfast FYI can be estimated with better accuracy using C-band SAR-derived copolarization ratio (f_{co}) than using only copolarized σ° at larger incidence angles. It was noted that the influence of deformation features, open water areas, and deeper melt ponds of pack ice and MYI on the validity of the r_{co} versus albedo relationship requires further investigations. Using a surface-based C-band polarimetric scatterometer data set, Scharien *et al.* [25] concluded that r_{co} has potential for the unambiguous detection of FYI melt pond formation and f_{mp} as it is unique from the background snow-covered or bare ice r_{co} as long as ponds are in liquid state. Cross-polarized σ° showed potential for discriminating the onset and duration of freeze events during the advanced melt in the marginal ice zone. The strong dependence of both co- and cross-polarized σ° on wind speed and pond depth was observed.

A model for f_{mp} retrieval over large MYI floes was developed by Jeffries *et al.* [31] for European Remote-Sensing Satellite-1 (ERS-1) SAR images. In this model, f_{mp} is derived by assuming the σ° of an MYI floe to be the linear sum of predetermined bare ice and melt pond σ° values. However, as the effect of wind roughening of melt pond surfaces was not taken into account as in [27], we think that the validity and accuracy of this model for different sea ice and wind conditions are limited.

Kern *et al.* [32] analyzed multifrequency σ° data acquired with a helicopter-borne scatterometer in the Arctic Ocean in late summer/early fall 2007. Results of a classification experiment with four different surface types, i.e., old ice, nilas, open water, and melt ponds, suggested that f_{mp} can be retrieved, but it depended on the microwave frequency combination used in the classification. The f_{mp} estimates were more realistic when frequencies like X- and Ku-bands were combined with C-band. Old ice and melt ponds showed similar C-band HH-polarization σ° signatures. Kim *et al.* [33] studied melt pond mapping with helicopter-borne very high resolution (0.3 m) X-band SAR data and a coincident TerraSAR-X stripmap mode image (6-m resolution). The helicopter-borne SAR can be used to map melt ponds at a level of detail comparable to aerial photography or high-resolution optical satellite images. Using the TerraSAR-X image, the detection of small melt ponds (< 130 m^2) was not possible, and f_{mp} was significantly underestimated compared to the helicopter-borne SAR results.

In summary, the current algorithms for f_{mp} estimation based on SAR data are basically linear fits between σ° and f_{mp} under different wind speeds, and only for landfast FYI with sufficient accuracy. Two studies with high resolution radar data [32], [33] showed that, even with high resolution (< 10 m) spaceborne SAR images, the detection of melt ponds is difficult and their fraction is underestimated if only single frequency and single polarization data are used. Thus, the prospects of successful f_{mp} estimation from the ENVISAT WSM images with single frequency (C-band), HH-polarization only, and coarse resolution (around 120 m) may be limited, but as a large image archive exists and new daily f_{mp} comparison data are available, it is worthwhile to study the possibilities.

II. Data Sets and Processing

In the following, the data sets for studying f_{mp} estimations from ENVISAT WSM images and their processing are described.

A. ENVISAT WSM Images

ENVISAT WSM images with HH-polarization were acquired for the study area shown in Fig. 1 for June–August 2009. The typical number of images per day is eight, and the total number of images in the data set is 705. The study area is not totally covered with the WSM images because the orbit inclination of the ENVISAT satellite limits the acquisition of the images up to about 87 N (denoted here as pole hole). The swath width of the WSM images is 406 km, the image length is variable (minimum of 400 km), the pixel size is 75 m, and the spatial resolution is around 113 $\times$ 123 m [34]. A WSM image consists of five subswaths with the following incidence angle (θ_0) ranges: SS1 16.3°–25.9°, SS2 25.9°–31.0°, SS3 31.0°–35.9°, SS4 35.9°–39.2°, and SS5 39.2°–42.7°. The whole θ_0 range is then from 16.3° to 42.7°.

The preprocessing of the WSM images consisted of georectification, calibration (absolute σ°), and land masking. The images were rectified to a polar stereographic coordinate system with a midlongitude of 0 E and a true-scale latitude of 70 N. The pixel size of the rectified images is 100 m. The equivalent number of looks (ENL) and noise equivalent $\sigma^\circ(\sigma^\circ_N)$ in the rectified images were studied using areas of calm water in the Barents Sea. The ENL is around 18 for the whole θ_0 range. Thus, the radiometric resolution is around 0.9 dB, and the standard deviation (std) of fading is 1.0 dB. σ°_N depends on the subswath, and it also changes as a function of θ_0 inside each subswath. For the SS1 subswath, σ°_N varies from -21 to -19 dB; for the subswaths SS2–SS4, it is -24.5 to -23 dB; and for the SS5, it ranges from -26 to -24.5 dB. The absolute accuracy of σ° is ± 0.63 dB [34].

The large θ_0 variation in the WSM images causes significant changes to the σ° level and contrast which complicates the successful implementation of sea ice classification algorithms. Thus, we applied a θ_0 compensation method to the images, following a method developed earlier for the Baltic Sea ice

[35]. For studying the θ_0 dependence of σ° in the study area, 25 windows of size 5.1 by 5.1 km were randomly selected over high IC regions. Next, θ_0 and σ° differences ($\Delta\theta_0$ and $\Delta\sigma^\circ$ in decibel scale) were calculated from image pairs acquired with less than one day time difference. The data were divided into weekly, half-monthly, and monthly intervals to study the effect of melt season progression in the σ° versus θ_0 dependence in different temporal scales. The scatter plots of σ° versus $\Delta\theta_0$ indicate a linear relationship between them, and thus, a linear regression model was fitted between them. The analysis of the slope terms showed that the monthly slope terms, i.e., -0.23 dB$/1^\circ$ in June, -0.25 dB$/1^\circ$ in July, and -0.20 dB$/1^\circ$ in August, are good approximations to follow the temporal behavior of the σ° versus θ_0 dependence. The coefficient of determination of the linear regressions for the monthly data varies from 0.79 to 0.94. Recently, also Zakhvatkina *et al.* [36] found the linear dependence between MYI σ° and θ_0 using WSM images and their slope term of -0.196 dB$/1^\circ$ for winter conditions is close to our results.

The incidence angle compensated WSM images (θ_0 normalized to 30°) were combined into a daily updated SAR image mosaic with 500-m pixel size; see examples in Fig. 2. The mosaic has a σ° range from -25.5 to 0 dB with 0.1-dB steps.

B. RGB Images From MODIS Level 1 B Data

Terra MODIS daytime L1B data with reflective 500-m bands were acquired for June–August 2009. There are typically 11 images per day for our study area. MODIS data were rectified to the polar stereographic coordinate system that we described earlier, keeping the original 500-m pixel size. Raw data from reflective bands were converted to top-of-the-atmosphere sun angle corrected reflectances. Two RGB images were calculated from the MODIS reflectance data: 1) bands 3-6-7 (RGB367) (this band combination is used for distinguishing between snow/ice and clouds) and 2) bands 2-1-3 (RGB213) (this band combination is suitable for the identification of flooded/wet sea ice, which can be identified by the bluish color in the images). These RGB images were used to evaluate qualitatively the accuracy of the cloud masking in the daily f_{mp} product and for the visual analysis of sea ice conditions.

C. MODIS Melt Pond Fraction Product

ICDC-processed daily melt pond fraction (f_{mp}) and open water fraction (f_{ow}) charts from a MODIS Surface Reflectance daily L2G Global product (MOD09GA) with 500-m pixel size. The f_{mp} and f_{ow} retrieval is based on different spectral behaviors of melt ponds compared to open water and snow and ice [8]. f_{mp} and f_{ow} are derived for each cloud-free 500-m pixel by applying a spectral unmixing algorithm presented in [12], which consists of a system of linear equations describing observed reflectances at MODIS bands 3 (459–479 nm), 1 (620–670 nm), and 2 (841–876 nm) as functions of areal fractions of three surface types, i.e., open water, melt ponds, and snow/ice, and their constant representative reflectances. An artificial neural network has been used to derive f_{mp} and f_{ow} from this set of equations [8]. The output data are gridded to a 12.5-km polar stereographic grid. The daily f_{mp} product has been validated with different data types from local observations

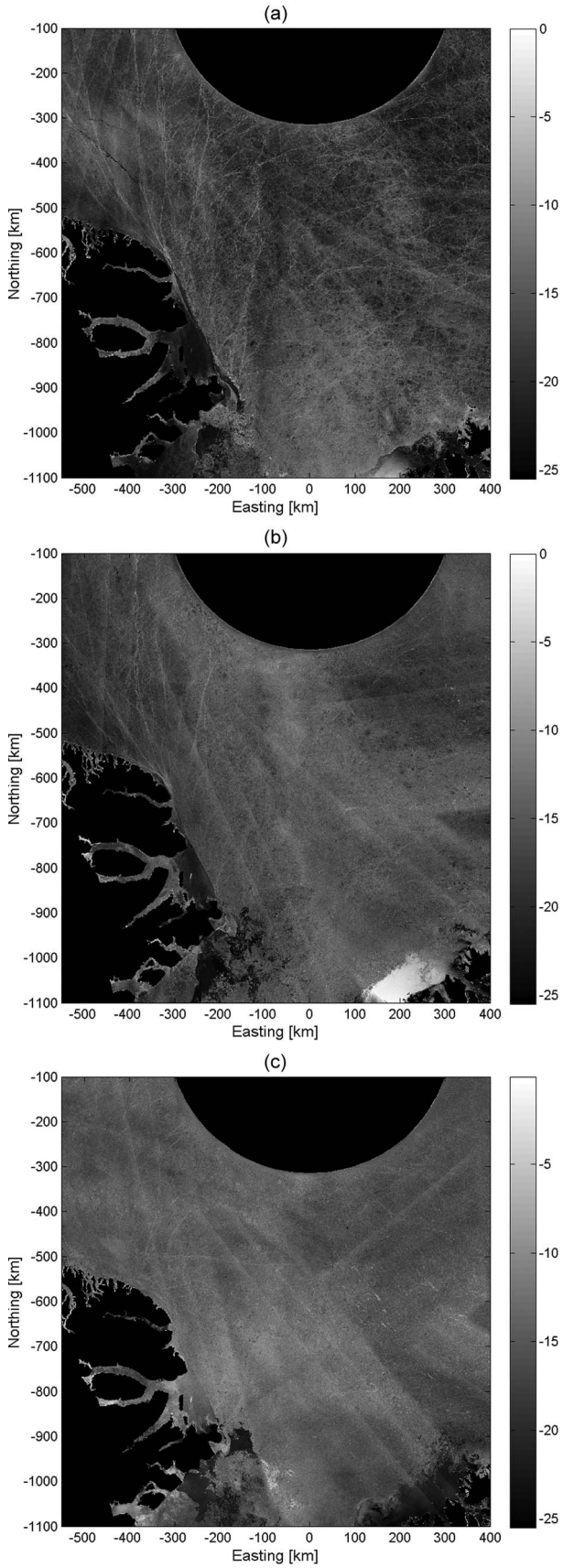

Fig. 2. Daily SAR mosaic from ENVISAT WSM images acquired on (a) July 4, (b) July 14, and (c) August 4, 2009. The backscattering coefficients in the mosaic are in decibel scale and scaled to the incidence angle of 30°. The pixel size is 500 m. The coordinate system is polar stereographic with a midlongitude of 0E.

(e.g., aerial photographs and ship observations) [8]. Root-mean-square errors between the f_{mp} product and validation f_{mp} varied from 3.8% to 11.2%.

We use here only those f_{mp} and f_{ow} 12.5-km grid cells which are based on at least 90% cloud-free 500-m pixels to increase reliability on the automatic cloud screening. The product was rectified to the study area with the nearest neighboring sampling and keeping the original 12.5-km grid resolution. Examples of f_{mp} charts are shown in Fig. 3.

The accuracy of the cloud mask in the f_{mp} charts was evaluated visually by comparing daily f_{mp} charts and series of RGB367 images of the same dates. The comparison shows that the f_{mp} charts include sometimes areas of undetected clouds and f_{mp} for these areas are typically either over- or underestimated when compared to neighboring cloud-free areas. However, the temporal analysis of f_{mp} in Section V-A shows that, despite this cloud masking error, the expected melt ponding and drainage periods are clearly identifiable in the f_{mp} time series. The cloud masking error only increases f_{mp} data scatter in the time series.

The accuracy of f_{mp} is additionally influenced by the limitations of the initial MODIS MOD09GA product. Due to the general lack of relevant atmospheric data for the Arctic region, potential sources of errors are to be assumed in the atmospheric correction and the influence of the viewing geometry and the solar angles. The bidirectional reflectance distribution function (BRDF) correction for most of the areas is based on modeled results for FYI and MYI. They are used as *a priori* estimates of the BRDF [8].

Submerged lateral areas of the ice floes may appear spectrally as melt ponds and reduce the accuracy of the melt pond product, but this effect is depending on the floe size and depending on the occurrence of a multiplicity of ice floes. The area of our investigations is covered mainly by thick MYI and FYI; therefore, we neglect the misclassification of submerged lateral areas of ice floes.

D. Weather Data

Weather station data were available from three DMI stations [37]; see Fig. 1. Weather observations (e.g., air temperature and wind speed) were conducted every hour or every 3 h. Weather data from the Kap Morris Jesup station were available after July 28, 2009, and those of the other two station were available for our entire study period.

Numerical weather prediction model data were extracted from ERA-Interim reanalysis data. ERA-Interim has four analyses per day, at 00, 06, 12, and 18 UTC. The parameters used here were 2-m air temperature (T_a) and 10-m U and V wind components. The data were retrieved at a 0.5° grid spacing. The spatial resolution is approximately 75 km. The data were rectified to the polar stereographic coordinate system of our study area with a 50-km grid resolution using cubic interpolation. Wind speed (V_a) was calculated from the U and V components.

E. IABP and NPEO Buoy Data

The position record data of the Arctic ice buoys are available from the IABP (data set C—daily buoy positions) [16]. Gridded

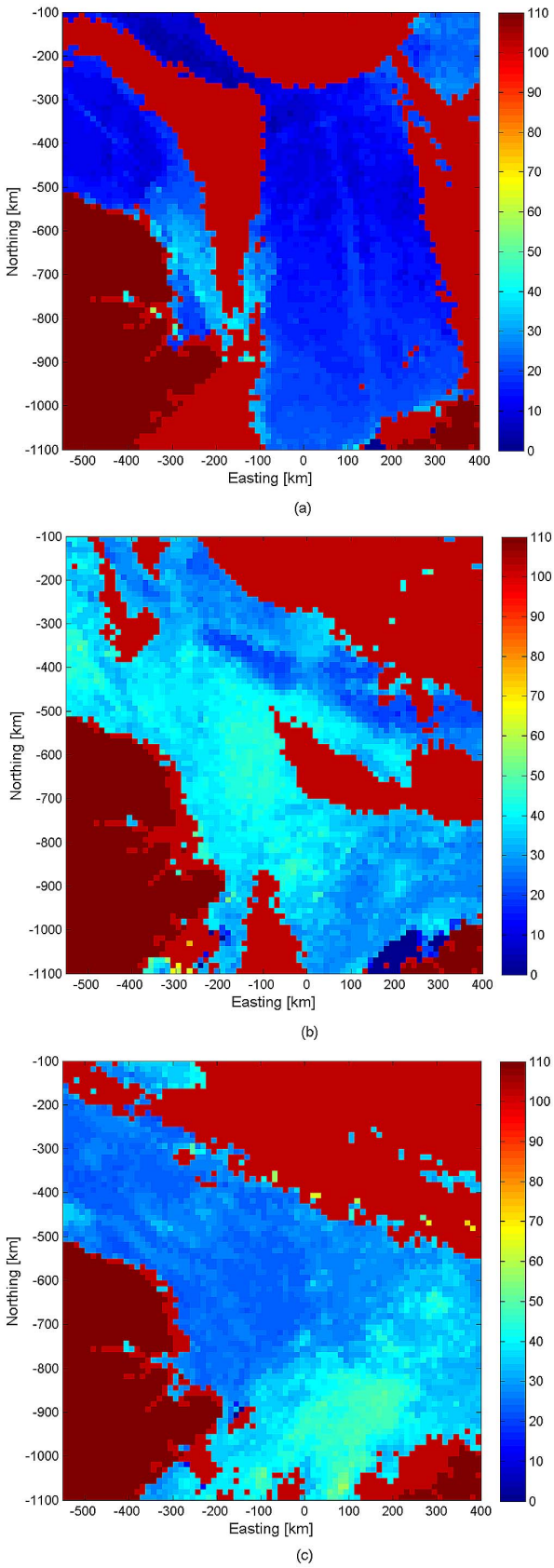

Fig. 3. MODIS melt pond fraction charts on (a) July 4, (b) July 14, and (c) August 4, 2009. The pixel size is 12.5 km. The land mask is shown with melt pond fraction of 110% and missing data, which can be clouds or open water areas, with 103%. The coordinate system is polar stereographic with a midlongitude of 0E.

12-hourly air pressure and T_a fields (data set AB) from buoy data have not yet been released for 2009. The position data are used for an overview of sea ice drift in our study area during June–August 2009 and for constructing f_{mp} and σ° time series where ice drift is tracked.

In summer 2009, the NPEO 2009 (http://psc.apl.washington.edu/northpole/index.html) drifted into our study area (see Fig. 1). NPEO included a Cold Regions Research and Engineering Laboratory ice mass balance (IMB) buoy 2009A [37], and its preliminary two-hourly data records are available (e.g., snow surface position and ice thickness). NOAA/Pacific Marine Environmental Laboratory (PMEL) weather station data with hourly records of T_a, pressure, near-surface wind speed (V_a), and station position are also available (ftp://psc.apl.washington.edu/NPEO_Data_Archive). There was also a webcam mounted on the PMEL weather station. Sea ice conditions interpreted visually from the webcam images are described in (http://www.arctic.noaa.gov/detect/ice-npole.shtml).

III. Methods

We study relationships between σ° and MODIS-derived f_{mp} with the following methods: 1) MODIS f_{mp} charts, MODIS RGB images, and SAR mosaic are visually compared to identify the increase and decrease of f_{mp} in the SAR mosaic; we analyze if these changes cause a distinguishable σ° change and texture, and this could give some guidelines for the analysis of the σ° versus f_{mp} relationship; 2) σ° and f_{mp} time series are extracted at the latitude–longitude grid points shown in Fig. 1 and along ice buoy tracks, and the aim is to detect significant σ° and f_{mp} (and other sea ice parameters) changes; and 3) Statistical relationships between σ° and f_{mp} are studied with spatially and temporally (daily) coincident σ° and f_{mp} data. As supporting information for these data analyses, sea ice thermodynamic state changes were estimated from ERA-Interim and weather station T_a data as in [39] and [21]. In the following, procedures for the data analyses 2) and 3) and for the thermodynamic state change estimation are discussed in detail.

A. Time Series of Melt Pond Fraction and Backscattering Coefficient

The time series of σ° and f_{mp} were extracted at the latitude–longitude grid points shown in Fig. 1; latitudes are 82N, 84N, and 86N, and the longitude is from -60E to $+40$E with either 20° (at 86N only) or 10° steps, if over ocean, and along the NPEO 2009 buoy and three IABP buoy tracks (ice drift tracked). These three IABP buoys had long position time series within our study area.

For the f_{mp} time series, windows with a size of 37.5×37.5 km^2 (3×3 12.5-km pixels) were centered at the grid points, and the buoy locations and the mean f_{mp} and f_{ow} were calculated if a window was totally cloud free.

σ° data were extracted from the WSM images (100-m pixel size) using a 25.1-km window (251×251 pixels) at the fixed grid points and a 12.5-km window centered at the buoy locations. From the window data, the following parameters were calculated: mean θ_0 and mean and std of σ° in decibel scale. To mitigate the effect of large scale ice features (e.g., ridges, hummocks, and leads) on the mean σ°, a large averaging window was used. The σ° time series along the buoy tracks are examples where the ice drift has been taken into account. In the other time series, we did not follow strictly the same area of ice but analyzed data from fixed latitude–longitude grid points. To diminish the effect of the large θ_0 variation (from 16.3° to 42.7°) in the σ° time series, they were first divided into two subswath categories, i.e., SS1 (16.3°–25.9°) and SS2–SS5 (25.9°–42.7°), and then scaled to the average incidence angles of 21° and 34°, respectively. For melt ponds, the σ° versus θ_0 dependence is larger than for snow covered and bare ice and also non-linear, and it is larger than that at larger incidence angles [25]. Thus, having two σ° time series with different θ_0 ranges should increase the accuracy of the θ_0 scaling. The number of samples in the time series ranges from 42 to 240, and the average is 137. The grid points along 86N have σ° data only where $> 35.5^\circ$ due to the proximity of the pole hole which means that this area can only be observed in the far θ_0 range of the WSM images.

It is possible to estimate the random variation in the θ_0-scaled σ° values due to the varying true σ° versus θ_0 dependence using the winter part of the σ° time series, when there are no significant temporal changes in sea ice characteristics. The random variation (σ°_{rv}) is characterized here by the std of the scaled σ° values. Parts of the time series with significant σ° trends in wintertime were visually excluded from the analysis.

B. Backscattering Coefficient Statistics Versus Melt Pond Fraction

For studying statistical relationships between σ° and f_{mp}, the σ° data from the WSM images and the MODIS f_{mp} and f_{ow} data were combined on a daily basis. First, centers of the 12.5-km MODIS grid cells with valid f_{mp} data (0%–100%) were mapped to the WSM images. Next, 12.5 km by 12.5 km σ° windows (125×125 100-m pixels) were extracted from the WSM images. For each SAR window, the mean θ_0 was calculated and assigned for all pixels within the window. From the σ° windows, the following parameters were calculated: mean σ°, std of σ°, modal σ° with 0.5-dB resolution, autocorrelation at lag one, interquartile range, skewness, kurtosis, mean of the highest one-third, and some textural features from the gray-level co-occurrence matrix (GLCM) [40], [41]: energy, contrast, correlation, homogeneity, entropy, cluster shade, and cluster prominence. ERA T_a and V_a were also extracted for the windows.

For the mean σ°, the effect of the θ_0 variation was compensated by either of the following: 1) scaling all σ° values to θ_0 of 30° or 2) first dividing the σ° data into two subswath categories, SS1 and SS2–SS5, and then scaling to the average θ_0's of 21° and 34°, respectively.

The textural feature energy (or angular second moment) is a measure of gray tone transitions. Correlation is a measure of the gray tone linear dependence in the image. Contrast is a measure of the intensity contrast between a pixel and its neighbor. Homogeneity measures the closeness of the distribution of elements in the GLCM to its diagonal. The two cluster parameters (shade and prominence) emulate human perceptual behavior. GLCM was calculated as an average of GLCMs at angles of 0° and 90° and with a distance (or offset) of one pixel.

The σ° data were quantized from -20.75 dB to -5 dB with a 0.25-dB resolution (64 gray levels). At the 100-m pixel size, the radiometric resolution is around 0.90 dB. We did not search an optimal quantization scheme and distance(s) as in [41].

In case of the mean σ° versus f_{mp} relationship, the effect of data resolution is briefly studied by using also averaging window sizes of 25, 50, and 100 km for both the σ° and f_{mp} data.

The number of SAR images for each day varies from 2 to 11, with an average of 8. The number of the 12.5-km SAR windows is, on the average, 4300 for each day, and the total number of windows is 391 407.

The MODIS f_{ow} was used to exclude SAR windows where the 100-m pixels typically represent either purely open water σ° signatures or have large open water contributions. As IC within pack ice is close to 100% and only at the ice edge substantially lower than 100%, we could set the f_{ow} limit to 20% and still retain 94% of the 12.5-km SAR windows.

C. Estimation of Sea Ice Thermodynamic State Changes

We estimated melt and freeze onsets from the ERA-Interim and weather station daily mean air temperature (T_{am}) by using a 2-week running median filter on the T_{am} time series and finding the days when the filtered data rise or drop below the -1 °C threshold chosen to represent the melting temperature of sea ice [21], [39].

IV. General Sea Ice Conditions

In summer 2009, most of the study area, north of the line Station Nord weather station—Northwest Svalbard, was covered with MYI and FYI with 30–200 cm in thickness with 9/10–10/10 IC according to the DMI weekly ice charts. Ice floes were classified in size categories of > 10 km, 2–10 km, and 0.5–2 km. South of the aforementioned line, the ice types and floe sizes were comparable to the north, but IC was slightly lower. The visual analysis of the SAR mosaic showed large open water areas only near Svalbard and south and southeast of the Henrik Krøyer Holme weather station (see Fig. 1). The ice edge was less than 100 km north of Svalbard. MYI and FYI pack ice was typically highly deformed with a dense network of ridges [see Fig. 2(a)]. Sea ice was generally drifting in southerly directions. The NPEO 2009 buoy drifted around 450 km during June 1–August 31 (see Fig. 1). In general, the ice drift was larger in the NE corner of the study area than in the NW one.

V. Results

In the following, we first analyze the changes of sea ice thermodynamic state and spatial and temporal behavior of the MODIS-derived f_{mp} in our study area in summer 2009 and then present results of our studies on the relationships between σ° and MODIS-derived f_{mp}.

A. Time Series of Sea Ice Thermodynamic State and Melt Pond Fraction

1) Sea Ice Thermodynamic States: In the study area (see Fig. 1), the melt onset varies from June 1, 2009 in the SE corner to June 16 in the NW corner according to the ERA-Interim median filtered T_{am} data [21], [39]. The average date for the melt onset is June 7. *In situ* T_{am} from the NPEO 2009 station was below 0 °C until July 4, and the median filtered T_{am} indicates melt onset on July 3. T_{am} from the two coastal stations, Henrik Krøyer Holme and Station Nord, shows melt onset on June 13 and 11, respectively. The NPEO 2009 IMB data show that snow pack with the initial thickness of around 50 cm started to melt at the end of June, and after 20 July, the snow thickness amounts to only a few centimeters. Thus, we assume that, within pack ice, at least the first week of June still represented winter ice conditions. The winter part of the σ° data is used to estimate the random variation in the θ_0-scaled σ° values due to the varying true σ° versus θ_0 dependence; see Section III-A.

The estimated freeze onset with the ERA T_{am} varies from August 15 to September 11 and with the mode of August 30. The NPEO 2009 T_{am} shows the freeze onset on August 31. At the three weather stations (from north to south order) Kap Morris Jesup, Station Nord, and Henrik Krøyer Holme, the freeze onset was August 28, September 1, and September 2, respectively. In general, the late August represented the start of the continuous freezing conditions.

2) Melt Pond Fractions: The only *in situ* data on f_{mp} in our study area are webcam images of the PMEL weather station of the NPEO 2009 (see Fig. 1 for the drift track). The visual analysis of the images is described in http://www.arctic.noaa.gov/detect/ice-npole.shtml. According to this analysis, melt ponds started to form on July 8, but they never became very widespread, with the maximum melt pond extent observed around July 14–16. Melt ponds were freezing over by August 11, but small slits of open water were still visible on September 8.

Fig. 4 shows f_{mp} and f_{ow} as a function of time from nine grid points along 84N. The general temporal f_{mp} trend is the following: f_{mp} increased slowly from around 10% to around 15% during June. Then, within the first two weeks of July, it increased rapidly to around 40%–45% (ponding period). The melt pond drainage period started around July 20–25, and f_{mp} decreased up to mid-August to around 25%. Afterward, f_{mp} did not decrease further. The rather large scatter in the f_{mp} time series reflects the variation of f_{mp} between the nine grid points which extend over a large geographical area.

During the first half of June which represents winter and early melt conditions, MODIS-derived f_{mp} was not 0% but between 5% and 15%. One possible explanation is that the surface reflectance used for snow/ice in the MODIS f_{mp} algorithm [8] does not exactly match the true sea ice reflectance in our study area which has highly deformed ice. The overestimation of low f_{mp} (below 10%) compared to validation data was typically observed in [8]. MODIS f_{ow} was typically below 5% until July 20 and then increased to 5%–20% in August, which, according to our qualitative visual analysis of the SAR mosaic, is somewhat too large. Without *in situ* data, it is difficult to find reasons for the f_{ow} level in August. In late summer, the MODIS f_{mp} algorithm likely has difficulties to distinguish open water from melt ponds which have melted through the ice. It is difficult therefore to say whether the lack of further decrease of f_{mp} after mid-August is a true trend or not. A multiyear mean

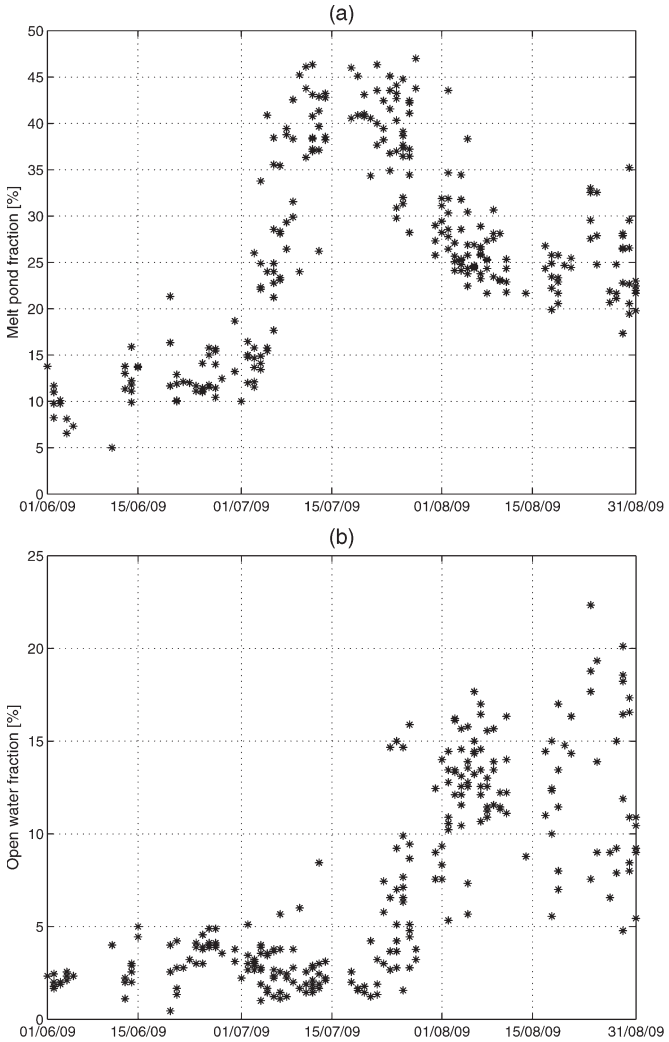

Fig. 4. (a) MODIS melt pond fraction and (b) open water fraction as a function of time extracted from nine latitude–longitude grid points along 84N (see Fig. 1).

f_{mp} for the entire Arctic from the 8-day MODIS product shows only a slight decreasing trend (from 30% to 25%) in August [42]. In the second half of August, atmospheric influences cause difficulties for the f_{mp} retrieval: f_{mp} might increase not only due to a real increase in melt pond coverage but also due to further ice melting. f_{mp} might decrease due to new ice formation in leads and on melt ponds. Snow fall on melt ponds already can create a few centimeters of thick slushlike ice cover, causing a substantial increase in reflectivity as observed by Kern *et al.* [43]. ERA daily mean T_a for the 84N grid points was above 0 °C until August 9, and after that, there were some freezing–melting cycles until August 29 after which the mean T_a was continuously below 0 °C. The data scatter in the f_{mp} time series does not allow a detection of freezing–melting cycles.

The f_{mp} and f_{ow} trends along the other two latitudes are similar. At 86N, the ponding period was slightly longer, and the 82N time series shows more data scatter, likely due to the proximity of the ice edge. In all f_{mp} time series, the daily absolute f_{mp} change is in 88% of the data below 5%. A few outliers up to 12% are observed, and they may be due to the cloud masking errors in the MODIS f_{mp} charts.

Along the NPEO 2009 buoy track (see Fig. 1), f_{mp} and f_{ow} have similar trends as in Fig. 4. The ponding period started after the first week of July. The peak f_{mp} with 45% was reached around July 22. Next, f_{mp} decreased until August 8 to around 20%–25%. In June and July, f_{ow} was below 5%, and in August, f_{ow} was 10%–20%. The visual analysis of the NPEO webcam imagery showed maximum melt pond extent around July 14–16. The main difference between the two data sets is the timing of the f_{mp} peak. However, there are no daily MODIS f_{mp} data for July 15–21, so the f_{mp} peak could have been earlier than on July 22.

We conclude that, despite some problems in the MODIS f_{mp} and f_{ow} data, overestimation at low f_{mp} values, and too large f_{ow} in late August, the data show clearly the expected melt ponding and drainage periods in our study area, and thus, it can be used for studying f_{mp} estimation from the ENVISAT WSM images.

B. Visual Analysis of SAR Mosaic With MODIS Melt Pond Fraction Charts and RGB Images

For the visual analysis of the increasing and decreasing f_{mp} in the SAR mosaics, we used MODIS f_{mp} chart and MODIS RGB images from July 1 when the ponding period was starting until the end of pond drainage (August 15). A selection of SAR mosaics (θ_0 normalized to 30°, 500-m pixel size) and comparable MODIS f_{mp} charts which contain large cloud-free areas from the aforementioned time period are shown in Figs. 2 and 3.

On July 4, f_{mp} was still low, with values in the center of the image ranging from 5% to 22% and an average of 15% [see Fig. 3(a)]. An area of larger f_{mp} near the NE coast of Greenland is likely due to cloud contamination in the f_{mp} retrieval. The RGB213 image (not shown) has a whitish tone in the middle of the image suggesting mainly snow-covered sea ice. In the SAR mosaic, a dense network of ice ridges is clearly visible [see Fig. 2(a)]. σ° has typically large spatial variation (texture), the std of σ° within a 12.5-km block is typically from 1.1 to 3.4 dB (90% variation interval), and the average is 2.1 dB. In comparison, the std of fading is around 1.0 dB.

On July 14, f_{mp} is now larger, its 90% variation interval is from 22% to 43% over the whole cloud-free area, and the average is 34%. The elongated area of low f_{mp} in the middle of Fig. 3(b) appears also in the f_{mp} chart for July 13. This feature is therefore a real f_{mp} anomaly and not a cloud masking error. The next cloud-free data set from this area is from July 22, and then, f_{mp} reaches values over 40%. The RGB213 image (not shown) has mainly a bluish tone indicating melt ponded ice or ice surface covered with a thin layer of liquid water. The SAR mosaic on July 14 [see Fig. 2(b)] shows less spatial σ° variation and typically larger σ° level than that on July 4, e.g., in the middle of the mosaic, ridges are not visible and the std of σ° is typically only 1.1–1.9 dB.

f_{mp} decreased rapidly after July 20 until mid-August. This period does not show clearly as a monotonous change of the σ° level and texture in the SAR mosaic. The only typically visible structures are the largest ridges and leads. The spatial variation of σ° is mostly small, e.g., the modal std of σ° for the mosaic of August 4 in Fig. 2(c) is only 1.2 dB. The area of the high f_{mp} in

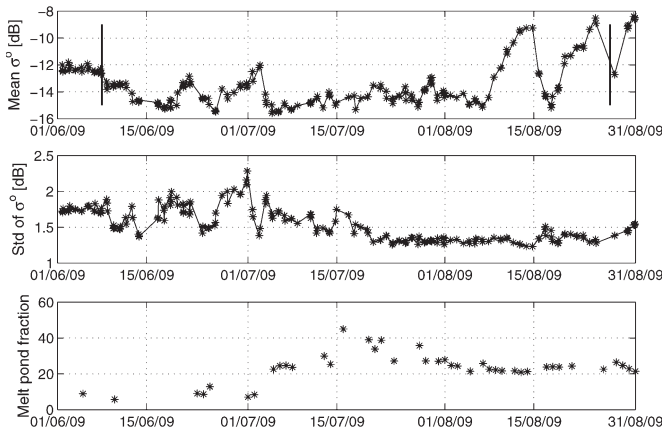

Fig. 5. Time series of mean and std of σ° (12.5-km window) and melt pond fraction (37.5-km window) at latitude–longitude grid point at 86 N, −40 E (see Fig. 1). σ° data are from the ENVISAT WSM subswaths SS2–SS5. Vertical lines are ERA-Interim daily mean T_a based melt and freeze onsets [21], [39].

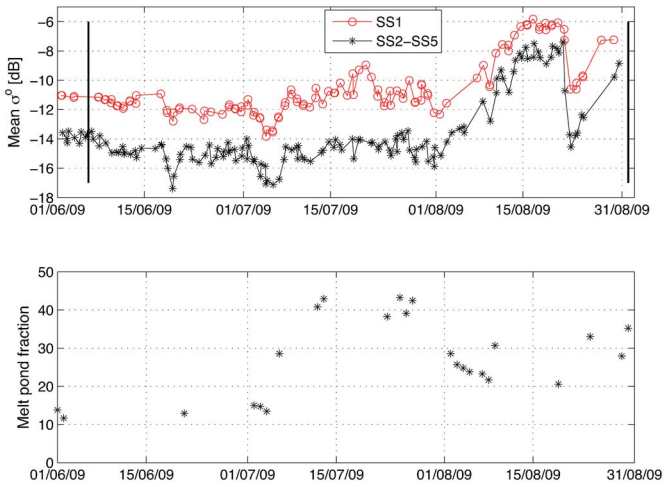

Fig. 6. Time series of mean σ° (12.5-km window) and melt pond fraction (37.5-km window) at latitude–longitude grid point at 84 N, 0 E (see Fig. 1). σ° data are from the ENVISAT WSM subswaths SS1 and SS2–SS5. Vertical lines are ERA-Interim daily mean T_a based melt and freeze onsets [21], [39].

the bottom of Fig. 3(c) is due to the unmasked clouds according to the RGB367 images of the same day. Outside this area, f_{mp} ranges from 20% to 35%, with an average of 25%.

In summary, during the ponding period, the texture of σ° decreases, and the average σ° level shows only a slight increase, whereas no monotonous σ° texture and level changes are visible in the drainage period. This suggests that the σ°-based derivation of f_{mp} is difficult and the accuracy may be poor.

C. Backscattering Coefficient and Melt Pond Fraction Time Series

First, we studied the random variation in the θ_0-scaled σ° values due to the varying true σ° versus θ_0 dependence using the winter part of the σ° time series. The random variation (σ°_{rv}) is characterized by the std of the scaled σ° values. Parts of the time series with significant σ° trends in wintertime were visually excluded from the analysis. σ°_{rv} varies from 0.2 to 0.5 dB, and the average is 0.3 dB. The maximum σ°_{rv} of 0.5 dB is used to identify significant σ° changes; an absolute σ° change between two successive values more than six hours apart and exceeding 0.5 dB is taken to be above the "noise" level of the θ_0 scaling. Large σ° changes within a shorter time interval are more likely due to the increased uncertainty of the θ_0 scaling when two consecutive σ° values have a large θ_0 difference.

In the following, two grid point σ° time series out of a total of 19 are studied in a more qualitative way to find out if significant σ° trends and changes correspond to changes in f_{mp}, T_a (ERA-Interim or *in situ*), and sea ice thermodynamic state. The first grid point is located at 86N, −40E (NE part of the study area), and denoted henceforth as gp1, and the second one is at 84N, 0E, denoted as gp12.

Fig. 5 shows the mean and std of σ° with subswath SS2–SS5 data and f_{mp} from gp1. Mean σ° time series with both SS1 and SS2–SS5 data, together with f_{mp} for gp12, are depicted in Fig. 6. The melt and freeze onset dates from the median-filtered ERA-Interim T_{am} are shown in the figures. In the gp1 σ° time series, the starting of the melting period corresponds to a gradual σ° decrease of 2–3 dB during the second week of June. The ERA T_{am}-derived melt onset was June 8. The σ° decrease in other time series varies from 1 to 5 dB. The σ° decrease from winter to melting conditions has been also observed, e.g., in [44] and [45].

In June–early July after the melt onset, some of the σ° time series have large σ° changes. For example, in Fig. 5, gp1 σ° increases by around 2.5 dB during June 18–22 and then decreases roughly the same amount up to June 26. A second large increasing–decreasing σ° event (around 3.5 dB) occurs during June 26 to July 4. Our first guess for the cause of these changes is atmospherically forced freezing–melting events. Freezing of snow and ice top layer would increase contributions of ice surface scattering from large scale roughness features (beneath the snow pack) and volume scattering from snow basal layer and ice top volume in the total σ°, and melting then decreases them. During the first event and since 8 June, ERA T_a was between −1.3 °C and +1.2 °C without any clear trends, but during the second event, T_a decreased from around 0 °C on June 26 to −1.5 °C in the morning of July 2 and then rapidly increased to +1 °C on July 4. Thus, it is possible that, at least the second event is due to a T_a change. However, it is also possible that these σ° changes are due to the ice drift which may change ice characteristics (e.g., ice type) at a fixed location. For example, on June 18–23, an IABP buoy (id 83725) near gp1 was drifting around 27 km but only in the northeast direction. The reversible nature of the σ° change (increasing–decreasing cycle) suggests the freezing–melting event as a more plausible explanation. Detailed *in situ* data would be needed for further studies. In June, the std of σ° is typically much larger than the std of speckle (around 1.0 dB) and has large temporal variations which are likely linked to changes of ice deformation, surface type (leads, FYI, and MYI), snow thickness, and wetness.

During the fast increase of f_{mp} in the first half of July (ponding period) at gp1 and gp1,2 there is also a gradual σ° (subswaths SS2–SS5) increase of roughly 2–3 dB. The σ° increase in the gp12 time series from the SS1 subswath is large, around 4 dB. At small θ_0, the separation between σ° for melt

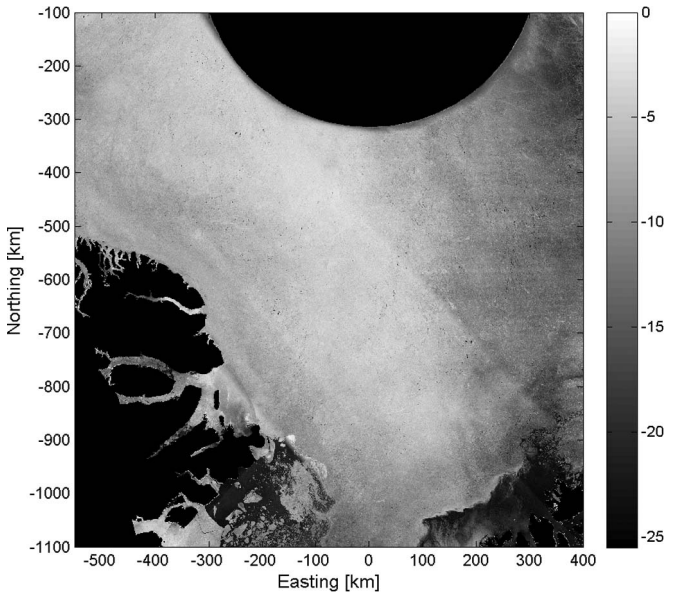

Fig. 7. Daily SAR mosaic from ENVISAT WSM images acquired on August 14, 2009 under freezing conditions. The backscattering coefficients in the mosaic are in decibel scale and scaled to the incidence angle of 30°. The pixel size is 500 m. The coordinate system is polar stereographic with a midlongitude of 0E.

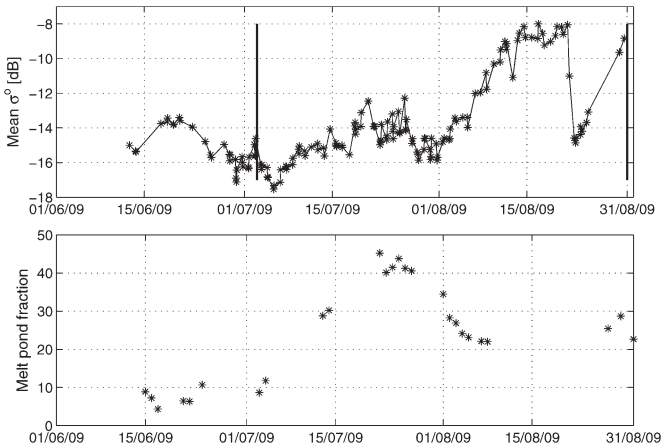

Fig. 8. Time series of mean σ° (12.5-km window) and melt pond fraction (37.5-km window) along the NPEO 2009 buoy track. σ° data are from the ENVISAT WSM subswaths SS2–SS5. Vertical lines are NPEO *in situ* daily mean T_a based melt and freeze onsets [21], [39].

ponds with rough surface and σ° for snow-covered or bare ice is larger than that at high θ_0 [25]. At these two grid points, the ERA V_a varied from 2 to 9 m/s at the times of the WSM image acquisitions. Yackel and Barber [27] found a significant positive linear relationship between σ° and f_{mp} over landfast FYI under windy conditions (around 5.3 m/s), but no relationship for light wind speeds ($\sim$1.5 m/s). In some other σ° time series at 86N and 84N and in all of 82N, there is no relationship between σ° and increasing f_{mp}.

Soon after the peak of f_{mp}, the drainage of the melt ponds started, and after the first week of August, a rather constant f_{mp} level, around 20%–30%, was reached at gp1 and gp12. This drainage period does not show as a clear monotonous increasing or decreasing σ° trend in our time series. This is the case also in all other σ° time series.

During the late drainage period in August, σ° time series have very large temporal variations. For example, at gp1, σ° increased by nearly 6 dB from August 6 to 14 and then decreased very rapidly by an equal amount until August 17. During this time, ERA T_a first decreased from around $+1$ °C to -2.5 °C on August 14 and then increased to $+0.5$ °C on August 17. T_a from the Kap Morris Jesup station (see Fig. 1) was above 0°C on August 4–8, and then, T_a decreased to -4 °C on August 8 followed by an increase to around $+3$ °C on August 17. The second increasing–decreasing σ° event occurred between August 18 and 28 also corresponding to a freeze–melt period. As these increasing–decreasing σ° events were present at all grid points, we think that they were caused by the freeze–melt events. The effect of these events on σ° is also illustrated by two SAR mosaics in Figs. 2(c) and 7. The first mosaic under melting conditions (August 4) has a lower level of σ° than the second mosaic under freezing conditions (August 14). In August, the std of σ° was mostly below 1.5 dB, indicating homogeneous backscattering conditions, and likely, surface scattering from wet ice/snow was dominating. The small spatial variation of σ° is evident in the mosaics. A possible explanation for the high σ° during freezing conditions is a strong volume scattering from the coarse grained snow-ice medium, e.g., [46]. In surface-based scatterometer measurements by Scharien *et al.* [25], bare ice had few decibels, and snow-covered ice had up to 5 dB larger σ° under freezing conditions than under melting conditions. Large σ° changes due to atmospheric forcing have also been observed for the Baltic Sea ice [23]. In our σ° time series, the ERA T_a based freeze onset date in late August typically matches with an increasing σ° trend.

The σ° and f_{mp} time series along the NPEO 2009 buoy track are depicted in Fig. 8. During the period of f_{mp} increase, also σ° increases, around 3–4 dB. The melt pond drainage period in late July shows a 2-dB drop in σ°, but as drainage continues in early August, the σ° increases by 7 dB until mid-August. In August, the NPEO buoy was close to gp12 which has a similar increasing σ° trend (see Fig. 6). The start of the σ° raise is around ten days later when the snow pack has melted to a few centimeters in thickness at the NPEO site. During August 1–15, *in situ* NPEO T_a shows only slight freezing periods on August 2–5 ($\min T_a - 1.5$ °C) and Aug 9–11 ($\min T_a - 1$ °C). It is difficult to find a plausible explanation for this increasing σ° trend. Maybe it is due to an increase of volume scattering as ice top surface is gradually drying up and slowly increasing in vertical extent as melt progresses. Another mechanism could be the surface scattering at melt pond edges which, as melt progresses, can develop a freeboard of several centimeters height. *In situ* wind speed was below 2 m/s, suggesting a smooth water surface and, thus, small scattering contribution from the melt ponds themselves. In the σ° time series for the three selected IABP buoys (one near gp1 and two close to the NE coast of Greenland), only at one (near gp1) did the f_{mp} increase in July result in an increasing σ° trend. Thus, it seems that the tracking of ice drift does not always increase the correlation between σ° and f_{mp}.

Finally, we studied visually scatterplots (not shown) between significant σ° changes ($|\Delta\sigma^\circ| > 0.5$ dB) and contemporary f_{mp}, T_a, and V_a changes. These plots did not show any correlation between the changes of the variables.

In summary, the detection of melt onset seems to be possible in the σ° time series based on the decreasing σ° trend from the winter σ° values. This was also reported in, e.g., [44] and [45]. The relationship between σ° and the increase of f_{mp} (ponding period) was typically not very clear; in some cases, a 2–3-dB σ° increase was present, but the trend was noisy with fast temporal variations mainly due to the "noise" of the θ_0 scaling and likely also from the varying roughness of the melt ponds. The relationship between σ° and f_{mp} was, in some cases, slightly better at smaller θ_0 values. The pond drainage period showed a σ° trend (decreasing) only in one case (NPEO buoy). The tracking of ice drift (buoy σ° time series) did not always improve the σ° versus f_{mp} relationship. Likely, in our study area ice deformation features and variation of ice types, upper ice volume characteristics, and snow thickness diminish σ° changes induced by melt ponding and drainage. In August when little snow remains and the MODIS f_{mp} shows a level of 20%–30% without any significant trends, there are large slow σ° variations likely linked to the atmospherically forced freezing–melting events. These events should also show up in brightness temperature signatures and, thus, possibly in the IC retrievals, which justifies their further study if detailed *in situ* data are available.

D. Backscattering Coefficient Statistics Versus Melt Pond Fraction

Here, we included data only from July 1 and August 5 which encompasses melt ponding and drainage periods. In June, MODIS-derived f_{mp} increases from about 10% to 15% and is likely overestimated as discussed in Section V-A. After August 5, there were large temporal σ° variations but small f_{mp} variations. The number of 12.5-km SAR windows is now 192 643.

First, we studied the relationship between f_{mp} and mean σ° for the 12.5-km windows. The scatterplot between f_{mp} and mean σ° values from all WSM swaths does not show any systematic relation between them. The correlation coefficient (r) is only 0.10 between the mean σ° and f_{mp}. The 90% interval of the ERA V_a in the data ranges from 1.3 to 8.6 m/s, and modal V_a is 3.5 m/s. Fig. 9 shows the scatterplot between f_{mp} and the SS1 subswath mean σ° values under three different ERA wind speed ranges: 0–3 m/s (calm light air), 4–7 m/s (light breeze), and larger than 8 m/s. Even though the separation between the melt pond and snow-covered or bare ice σ° values should be larger at the smaller θ_0's [25] (SS1 subswath), r between f_{mp} and mean σ° is not much larger; it is, at best, 0.30 under the 4–7-m/s wind speed range.

The effect of resolution on the relationship between f_{mp} and the mean σ° was briefly studied using also averaging windows of 25, 50, and 100 km for the both data sets. This further spatial averaging did not increase the correlation between the f_{mp} and mean σ°, regardless of the wind speed range.

Next, the mean σ° probability density functions (pdfs) were calculated for 5% wide f_{mp} intervals (5%–9%, 10%–14%, etc.) using the data from the 12.5-km size windows. Fig. 10 shows pdfs with mean σ° values from all WSM subswaths. The number of samples for each pdf is, at minimum, 443, and the average is 17 475. The σ° pdfs for different f_{mp} intervals for f_{mp} larger than 25% do not differ much from each other. The

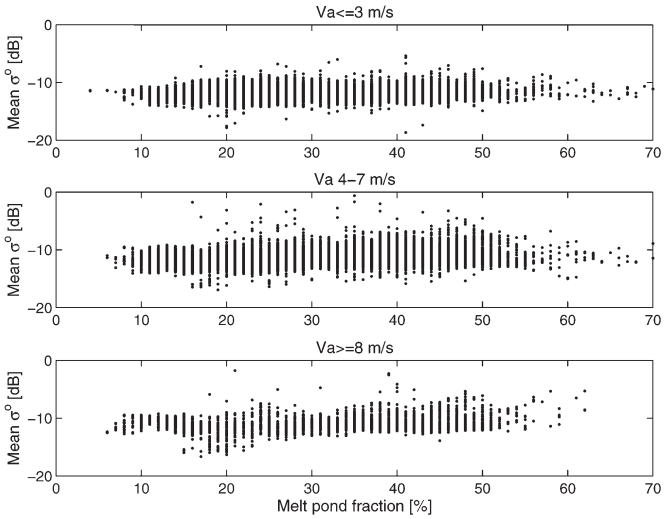

Fig. 9. Scatterplot between the melt pond fraction and the mean σ° at 12.5-km pixel size under three different ERA-Interim wind speed ranges. All σ° data are from the WSM subswath SS1 and the incidence angle scaled to 21°. Only data from July 1 to August 5, 2009 are used. MODIS open water fraction is below 20%.

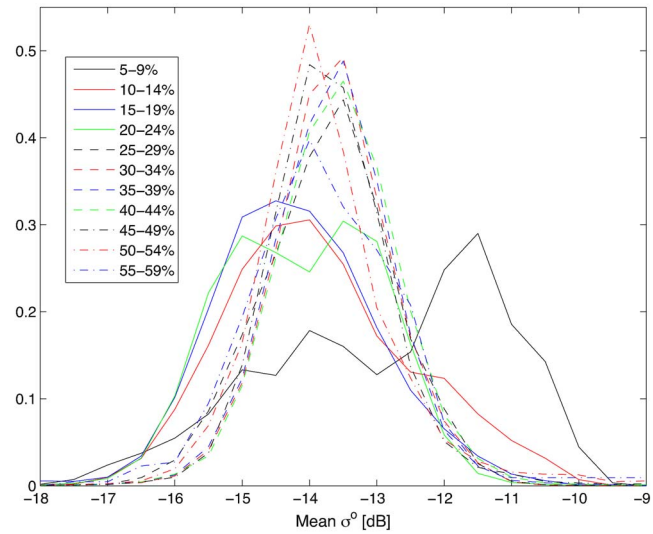

Fig. 10. PDFs of the mean σ° values at 12.5-km pixel size for different melt pond fraction intervals. Only data from July 1 to August 5, 2009 are used. MODIS open water fraction below 20%. The bin width of pdfs is 0.5 dB.

pdfs for f_{mp} intervals of 10%–14%, 15%–19%, and 20%–24% have a somewhat larger proportion of smaller σ° values than the pdfs for larger f_{mp}. Only the pdf for the f_{mp} interval of 5%–9% clearly differs from the rest; its peak position is on a 2–3-dB larger σ° value than the peaks of other pdfs. All σ° data for this pdf were acquired on July 1–4, when the areas with f_{mp} between 5%–9% were north of Greenland and had rather high average σ° due to freezing conditions; see σ° time series in Fig. 5. The separation of pdfs does not improve by restricting the θ_0 range (SS1 or SS2–SS5). Mean σ° values from all WSM subswaths range only from -17 to -10 dB, regardless of the f_{mp} interval.

In summary, using σ° data block averaged to the same pixel size as the MODIS f_{mp} data (12.5 km), it is not possible to estimate f_{mp}. Very likely, at this coarse spatial resolution,

other properties of sea ice, mainly ice deformation features and mixtures of various ice types (e.g., MYI floes and brash ice), are masking σ° variations by changing f_{mp}, as was also suggested in the σ° time series study. For better studying the relationship between σ° level and f_{mp}, we need f_{mp} data at higher resolution. Yackel and Barber [27] used their study RADARSAT-1 SAR data averaged to a 500-m pixel size and fine-resolution ($\sim$16.5m^2) aircraft video-based f_{mp} data and found good correlation between σ° and f_{mp} for smooth landfast FYI under windy conditions (around 5.3 m/s).

Finally, we studied the relationships between f_{mp} and various statistical (e.g., std, mode, and autocorrelation) and GLCM texture features (see Section III-B) calculated from the 12.5-km SAR σ° windows with 100-m pixel size. None of the parameters has a significant relationship with f_{mp}, and their pdfs do not differ significantly for different f_{mp} intervals, regardless of the incidence angle range selection (all subswaths, SS1, or SS2–SS5).

VI. Conclusion

We have studied f_{mp} estimation over the Arctic MYI and FYI using ENVISAT WSM images acquired over an area north of the Fram Strait, Greenland, and Svalbard. Melt pond and open water fraction data were available from ICDC's daily MODIS melt pond product with a 12.5-km pixel size [8]. Data sets were acquired for June–August 2009.

The MODIS f_{mp} data showed expected melt ponding and drainage periods in our study area. f_{mp} increased from about 10% to 15% in June. Within the first two weeks of July, it increased rapidly to around 40%–45% (ponding period) and then decreased up to mid-August to around 25% (drainage period). Afterward, f_{mp} did not decrease further. The nonzero f_{mp} in the beginning of June may be due to a slight mismatch of surface reflectance for snow/ice used in the MODIS f_{mp} algorithm for our study area with highly deformed ice. The overestimation of low f_{mp} (below 10%) compared to validation data was typically observed by Rösel *et al.* [8]. It is difficult to say whether the stagnation of f_{mp} after mid-August is a real trend or not. A multiyear mean f_{mp} for the whole Arctic from the 8-day MODIS product showed only a slight decreasing trend (from 30% to 25%) in August [42]. We note that melting and freezing coexist at that time of the year and that other effects than actual changes in absolute melt pond area can contribute to the temporal development of f_{mp}. ERA T_a suggests freezing–melting cycles in August which could have slowed the melt pond drainage.

Possible relationships between SAR σ° and MODIS f_{mp} were studied visually by comparing daily SAR mosaics and f_{mp} charts and MODIS RGB images and by analyzing f_{mp} and σ° time series and spatially and temporally coincident f_{mp} and σ° data from 12.5-km windows. The θ_0 range for the σ° data was either that for the SS1 subswath (16.3°–25.9°), SS2–SS5 swaths (25.9°–42.7°), or all WSM swaths (16.3°–42.7°). Overall, the results showed only little correspondence between the increase and decrease of f_{mp} and the σ° statistics (mean, std, and other texture parameters), Therefore, the f_{mp} estimation from the WSM images is not possible, at least in our data sets. In some cases, there was a 2–3-dB σ° increase during the ponding period, but the trend had fast temporal variations due to the "noise" of the θ_0 scaling in σ° and likely also from the varying roughness of the melt pond surface due to changing wind conditions. The relationship between σ° and f_{mp} was, in some cases, slightly better at smaller θ_0. The tracking of ice drift with the ice buoy data did not significantly improve the σ° versus f_{mp} relationship. Likely, in our study area, ice deformation features, variation of ice types, upper ice volume characteristics, and snow pack diminish both σ° level changes at 12.5-km resolution and textural σ° changes at 100-m resolution due to the melt ponding and drainage.

Previously, good correlation between σ° and f_{mp} has only been observed for smooth landfast FYI [27]. Studies with high resolution radar data [32], [33] showed that, even with high resolution (< 10 m), spaceborne SAR image detection of melt ponds is difficult and f_{mp} is underestimated if only single frequency and single polarization data are used. Nevertheless, it may be worthwhile to repeat our study if high-resolution f_{mp} data sets, at least with resolution comparable to the typical 50–100-m resolution of wide swath SAR images (e.g., RADARSAT-2 ScanSAR), with large spatial and temporal coverage become available and, better yet, if these are accompanied with high-resolution sea ice albedo data. Statistically, σ° may be more closely related to the albedo than to f_{mp} as albedo results from the integration of all surface types (snow, bare ice, and melt ponds) which contribute to the measured σ°[27]. If an algorithm for the f_{mp} or albedo estimation over the Arctic drift ice can be developed then f_{mp} or albedo products could be calculated from a large ENVISAT WSM and RADARSAT-1/2 ScanSAR image archive over the Arctic Sea ice. The large θ_0 variation in the WSM images is a problem in the σ° analysis and image classification, as it can be compensated for only partially. Because melt ponds are mostly smaller than the WSM image resolution of 100 m, leading to mixed pixel σ° signatures, a future study should also include fine-resolution ($< 10-20$ m) SAR images with limited θ_0 ranges, preferably with two copolarizations (HH and VV). According to surface-based C-band scatterometer measurements, the copolarization ratio has potential for unambiguous detection of FYI melt pond formation and f_{mp} [25].

A very interesting observation was the large typically long-term temporal σ° variation during the late melting season in August when little snow remains and the MODIS f_{mp} was based at a level of 20%–30% without any systematic variations. These σ° variations are very likely linked to the atmospherically forced freeze–melt events. A plausible explanation for high σ° in freezing conditions is strong volume scattering from the coarse grained snow-ice medium. These events should also show in brightness temperature signatures and, thus, possibly in the radiometer IC retrievals, which justifies their further study, if detailed *in situ* data become available.

References

[1] D. K. Perovich, S. V. Nghiem, T. Markus, and A. Schweiger, "Seasonal evolution and interannual variability of the local solar energy absorbed by the arctic sea ice—Ocean system," *J. Geophys. Res.*, vol. 112, no. C3, pp. C03005-1–C03005-13, Mar. 2007.

[2] M. Nicolaus, C. Katlein, J. Maslanik, and S. Hendricks, "Changes in arctic sea ice result in increasing light transmittance and absorption," *Geophys. Res. Lett.*, vol. 39, no. 24, pp. L24501-1–L24501-6, Dec. 2012.

[3] H. Eicken, T. C. Grenfell, D. K. Perovich, J. A. Richter-Menge, and K. Frey, "Hydraulic controls of summer arctic pack ice albedo," *J. Geophys. Res.*, vol. 109, no. C8, pp. C08007-1–C08007-12, Aug. 2004.

[4] D. K. Perovich, W. B. Tucker, III, and K. A. Ligett, "Aerial observations of the evolution of ice surface conditions during summer," *J. Geophys. Res.*, vol. 107, no. C10, pp. SHE 24-1–SHE 24-14, Oct. 2002.

[5] D. J. Cavalieri, B. A. Burns, and R. G. Onstott, "Investigation of the effects of summer melt on the calculation of sea ice concentration using active and passive microwave data," *J. Geophys. Res.*, vol. 95, no. C4, pp. 5359–5369, Apr. 1990.

[6] C. A. Pedersen, E. Roeckner, M. Luethje, and J.-G. Winther, "A new sea ice albedo scheme including melt ponds for ECHAM5 general circulation model," *J. Geophys. Res.*, vol. 114, no. D8, pp. D08101-1–536D08101-15, Apr. 2009.

[7] D. Flocco, D. Schroeder, D. L. Feltham, and E. C. Hunke, "Impact of melt ponds on Arctic sea ice simulations from 1990 to 2007," *J. Geophys. Res.*, vol. 117, no. C9, pp. C09032-1–C09032-17, Sep. 2012.

[8] A. Rösel, L. Kaleschke, and G. Birnbaum, "Melt ponds on arctic sea ice determined from MODIS satellite data using an artificial neural network," *Cryosphere*, vol. 6, no. 2, pp. 431–446, Apr. 2012.

[9] J. C. Comiso and R. Kwok, "Surface and radiative characteristics of the summer arctic sea ice cover from multisensory satellite observation," *J. Geophys. Res.*, vol. 101, no. C12, pp. 28 397–28 416, Dec. 1996.

[10] F. Fetterer and N. Untersteiner, "Observations of melt ponds on arctic sea ice," *J. Geophys. Res.*, vol. 103, no. C11, pp. 24 821–24 835, Oct. 1998.

[11] T. Markus, D. J. Cavalieri, M. A. Tschudi, and A. Ivanoff, "Comparison of aerial video and Landsat 7 data over ponded sea ice," *Remote Sens. Environ.*, vol. 86, no. 4, pp. 458–469, Aug. 2003.

[12] M. A. Tschudi, J. A. Maslanik, and D. K. Perovich, "Derivation of melt pond coverage on arctic sea ice using Modis observation," *Remote Sens. Environ.*, vol. 112, no. 5, pp. 2605–2614, May 2008.

[13] A. Rösel, L. Kaleschke, and S. Kern, "Gridded melt pond cover fraction on arctic sea ice derived from TERRA-MODIS 8-day composite reflectance data," Hamburg, Germany, 2013.

[14] R. A. Frey, S. A. Ackerman, Y. Liu, K. I. Strabala, H. Zhang, J. R. Key, and X. Wang, "Cloud detection with MODIS. Part I: Improvements in the MODIS cloud mask for collection 5," *J. Atmos. Ocean. Technol.*, vol. 25, no. 7, pp. 1057–1072, Jul. 2008.

[15] M. A. Chan and J. C. Comiso, "Arctic cloud characteristics as derived from MODIS, CALIPSO, and CloudSat," *J. Clim.*, vol. 26, no. 10, pp. 3285–3306, May 2013.

[16] I. G. Rigor, "IABP drifting buoy pressure, temperature, position, and interpolated ice velocity," National Snow and Ice Data Center, Boulder, CO, USA, 2002, [Jun.–Aug. 2009].

[17] C. E. Livingstone, R. G. Onstott, L. D. Arsenault, A. L. Gray, and K. P. Singh, "Microwave sea-ice signatures near the onset of melt," *IEEE Trans. Geosci. Remote Sens.*, vol. GE-25, no. 2, pp. 174–187, Mar. 1987.

[18] D. G. Barber, J. J. Yackel, and J. M. Hanesiak, "Sea ice, RADARSAT-1 and arctic climate processes: A review and update," *Can. J. Remote Sens.*, vol. 27, no. 1, pp. 51–61, 2001.

[19] T. Markus, J. C. Stroeve, and J. Miller, "Recent changes in arctic sea ice melt onset, freezeup, and melt season length," *J. Geophys. Res.*, vol. 114, no. C12, pp. C12024-1–C12024-14, Dec. 2009.

[20] L. Wang, G. J. Wolken, M. J. Sharp, S. E. L. Howell, C. Derksen, R. D. Brown, T. Markus, and J. Cole, "Integrated pan—Arctic melt onset detection from satellite active and passive microwave measurements, 2000–2009," *J. Geophys. Res.*, vol. 116, no. D22, pp. D22103-1–D22103-15, Nov. 2011.

[21] J. Mortin, T. M. Schrøder, A. Walløe Hansen, B. Holt, and K. C. McDonald, "Mapping of seasonal freeze-thaw transitions across the pan-arctic land and sea ice domains with satellite radar," *J. Geophys. Res.*, vol. 117, no. C8, pp. C08004-1–C08004-19, Aug. 2012.

[22] J. J. Yackel, D. G. Barber, T. N. Papakyriakou, and C. Breneman, "First-year sea ice spring melt transitions in the Canadian Arctic Archipelago from time-series synthetic aperture radar data, 1992–2002," *Hydrol. Process.*, vol. 21, no. 2, pp. 253–265, Jan. 2007.

[23] M. Mäkynen, B. Cheng, M. Similä, T. Vihma, and M. Hallikainen, "Comparisons between SAR backscattering coefficient and results of a thermodynamic snow/ice model for the Baltic Sea land-fast sea ice," *IEEE Trans. Geosci. Remote Sens.*, vol. 45, no. 5, pp. 1131–1141, May 2007.

[24] M. R. Drinkwater, "LIMEX'87 ice surface characteristics: Implications for C-band SAR backscatter signatures," *IEEE Trans. Geosci. Remote Sens.*, vol. 27, no. 5, pp. 501–513, Sep. 1989.

[25] R. K. Scharien, J. J. Yackel, D. G. Barber, M. Asplin, M. Gupta, and D. Isleifson, "Geophysical controls on C band polarimetric backscatter from melt pond covered arctic first-year sea ice: Assessment using high-resolution scatterometry," *J. Geophys. Res.*, vol. 117, no. C9, pp. C00G18-1–C00G18-15, Sep. 2012.

[26] R. K. Scharien and J. J. Yackel, "Analysis of surface roughness and morphology of first-year sea ice melt ponds: Implications for microwave scattering," *IEEE Trans. Geosci. Remote Sens.*, vol. 43, no. 12, pp. 2927–2939, Dec. 2005.

[27] J. J. Yackel and D. G. Barber, "Melt ponds on sea ice in the Canadian Arctic Archipelago. Part 2. On the use of RADARSAT-1 synthetic aperture radar for geophysical inversion," *J. Geophys. Res.*, vol. 105, no. C9, pp. 22 061–22 070, Sep. 2000.

[28] D. G. Barber and J. J. Yackel, "The physical, radiative and microwave scattering characteristics of melt ponds on arctic landfast sea ice," *Int. J. Remote Sens.*, vol. 20, no. 10, pp. 2069–2090, Jan. 1999.

[29] J. Hanesiak, J. Yackel, and D. Barber, "Effect of melt ponds on first-year sea ice ablation—Integration of RADARSAT-1 and thermodynamic modeling," *Can. J. Remote Sens.*, vol. 27, no. 5, pp. 433–442, 2001.

[30] R. K. Scharien, J. J. Yackel, M. A. Granskog, and B. G. T. Else, "Coincident high resolution optical-SAR image analysis for surface albedo estimation of first-year sea ice during summer melt," *Remote Sens. Environ.*, vol. 111, no. 2/3, pp. 160–171, Nov. 2007.

[31] M. O. Jeffries, K. Schwartz, and S. Li, "Arctic ocean melt season characteristics and sea ice melt pond fractions using ERS-1 SAR," in *Proc. 4th Symp. Remote Sens. Polar Environ.*, 1996, pp. 127–132, ESA SP-391.

[32] S. Kern, M. Brath, and D. Stammer, "Melt ponds as observed with a helicopter-borne, multi-frequency scatterometer in the Arctic Ocean in 2007," presented at the European Space Agency Living Planet Symp., Bergen, Norway, Jun. 29–Jul. 2, 2010, ESA-SP-686.

[33] D.-J. Kim, B. Hwang, K. H. Chung, S. H. Lee, H.-S. Jung, and W. M. Moon, "Melt pond mapping with high-resolution SAR: The first view," *Proc. IEEE*, vol. 101, no. 3, pp. 748–758, Mar. 2013.

[34] "ENVISAT ASAR monthly report," Paris, France, ENVI-CLVL-EOPG-TN-04-0009, Jun. 2009, Technical note.

[35] M. Mäkynen, A. T. Manninen, M. Similä, J. Karvonen, and M. Hallikainen, "Incidence angle dependence of the statistical properties of C-band HH-polarization backscattering signatures of the Baltic Sea ice," *IEEE Trans. Geosci. Remote Sens.*, vol. 40, no. 12, pp. 2593–2605, Dec. 2002.

[36] N. Y. Zakhvatkina, V. Y. Alexandrov, O. M. Johannessen, and S. Sandven, "Classification of sea ice types in ENVISAT synthetic aperture radar images," *IEEE Trans. Geosci. Remote Sens.*, vol. 51, no. 5, pp. 2587–2600, May 2013.

[37] "Weather and climate data from Greenland 1958–2011—Observation data with description," Danish Meteorol. Inst., Copenhagen, Denmark, DMI Tech. Rep. 12-15, 2012, J. Cappalen (editor).

[38] D. K. Perovich, J. A. Richter-Menge, B. Elder, K. Claffey, and C. Polashenski, Observing and Understanding Climate Change: Monitoring the Mass Balance, Motion, and Thickness of Arctic Sea Ice, 2009. [Online]. Available: http://imb.crrel.usace.army.mil/

[39] I. G. Rigor, R. L. Colony, and S. Martin, "Variations in surface air temperature observations in the Arctic, 1979–97," *J. Clim.*, vol. 13, no. 5, pp. 896–914, Mar. 2000.

[40] J. A. Nystuen and F. W. Garcia, Jr., "Sea ice classification using SAR backscatter statistics," *IEEE Trans. GeoSci. Remote Sens.*, vol. 30, no. 3, pp. 502–509, May 1992.

[41] L. K. Soh and C. Tsatsoulis, "Texture analysis of SAR sea ice imagery using gray level co-occurrence matrices," *IEEE Trans. Geosci. Remote Sens.*, vol. 37, no. 2, pp. 780–795, Mar. 1999.

[42] A. Rösel and L. Kaleschke, "Exceptional melt pond occurrence in the years 2007 and 2011 on the arctic sea ice revealed from MODIS satellite data," *J. Geophys. Res.*, vol. 117, no. C5, pp. C05018-1–C05018-8, May 2012.

[43] S. Kern, G. Spreen, and A. Winderlich, "Sea ice radar backscatter measurements for improved melt pond and thin-ice cover analysis," in *The Expedition ARKTIS-XXII/2 of the Research Vessel "Polarstern"*, vol. 579, *Reports on Polar and Marine Research*, U. Schauer, Ed. Bremerhaven, Germany: Alfred Wegener Institute for Polar and Marine Research, 2008, 271.

[44] D. P. Winebrenner, E. D. Nelson, R. Colony, and R. D. West, "Observations of melt onset on multi-year arctic sea ice using the ERS-1 SAR," *J. Geophys. Res.*, vol. 99, no. C11, pp. 22 425–22 442, Nov. 1994.

[45] R. Kwok, G. F. Cunningham, and S. V. Nghiem, "A study of the onset of melt over the arctic ocean in RADARSAT synthetic aperture radar data," *J. Geophys. Res.*, vol. 108, no. C11, pp. 27-1–27-13, Nov. 2003.

[46] A. Carlström and L. M. H. Ulander, "C-Band backscatter signatures of old sea ice in the central arctic during freeze-up," *IEEE Trans. Geosci. Remote Sens.*, vol. 31, no. 4, pp. 819–829, Jul. 1993.

Marko Mäkynen (S'98–M'01) received the Dr.Sci. (Technology) degree from the Helsinki University of Technology (TKK), Espoo, Finland, in 2007.

Since 2009, he has been a Senior Scientist at the Marine Research Unit of the Finnish Meteorological Institute, Helsinki, Finland. He was a Senior Teaching Assistant at the Laboratory of Space Technology, TKK, in 1999–2006 and was the Acting Director of the laboratory in 2007–2008. His main research interest is microwave and optical remote sensing of the Baltic and Arctic Sea ice.

Stefan Kern received the Diploma degree in meteorology from the University of Hannover, Hannover, Germany, in 1997 and the Ph.D. degree in physics from the University of Bremen, Bremen, Germany, in 2001.

Since 2001, he has been with the University of Hamburg, Hamburg, Germany, where he first worked in the Institute of Oceanography and where he joined the Center of Excellence for Climate System Analysis and Prediction in 2010, which now is part of the Zentrum für Erdsystemforschung und Nachhaltigkeit. His main research interests are remote sensing of the marine cryosphere, algorithm development, and uncertainty assessment for improved quantification of ocean–sea-ice–atmosphere interactions. He carried out field experiments measuring multifrequency radar backscatter of Arctic sea ice and Alpine snow using a helicopter-borne scatterometer. He currently dedicates his work to sea-ice-related climate data record uncertainty assessment.

Anja Rösel was born in in Munich, Germany, on April 22, 1976. She received the Dr.Nat.Sci. degree from the Institute of Oceanography, University of Hamburg, Hamburg, Germany, in 2012.

Since 2013, she has obtained a fellowship of the Young Researcher's Initiative of the University of Hamburg. She studied physical geography with main focus on climatology and remote sensing at the University of Munich, Munich. From 2005 to 2007, she was a member of the wintering team of the German Neumayer Research Station in Antarctica and was responsible for the Meteorological Observatory. After the wintering, she started her Ph.D. at the University of Hamburg, investigating in the detection of melt ponds from optical satellite data. Her main research interest is remote sensing of the polar regions.

Leif Toudal Pedersen was born in Denmark in 1957. He received the M.S. degree in microwave engineering and the Ph.D. degree in passive microwave remote sensing of sea ice from the Technical University of Denmark (TUD), Kongens Lyngby, Denmark, in 1982 and 1992, respectively.

From 1982 to 2000, he was a Research Assistant at the Electromagnetics Institute at TUD, and from 2000 to 2007, he was an Associate Professor at Ørsted-TUD, Denmark. Since 2007, he has been a Senior Researcher at the Center for Ocean and Ice at the Danish Meteorological Institute. His research interests include the retrieval of ice, ocean, and atmospheric parameters from multispectral microwave radiometer measurements as well as other methods for remote sensing of sea ice.

Dr. Pedersen is a member of the Danish National Committee for Climate Research and the Danish National Committee for Scientific Committee on Antarctic Research. He also serves as a Danish delegate to European Space Agency's Programme Board for Earth Observations and on ESA's Sentinel-1 Mission Advisory Group.